Correlated Three-Dimensional Imaging of Dislocations: Insights into the Onset of Thermal Slip in Semiconductor Wafers

D. Hänschke,[1,2,*] A. Danilewsky,[3] L. Helfen,[1,4] E. Hamann,[1] and T. Baumbach[1,2]
[1]*Karlsruhe Institute of Technology (KIT), Institute for Photon Science and Synchrotron Radiation (IPS), 76344 Eggenstein-Leopoldshafen, Germany*
[2]*Karlsruhe Institute of Technology (KIT), Laboratory for Applications of Synchrotron Radiation (LAS), 76128 Karlsruhe, Germany*
[3]*Kristallographie, Institut für Geo- und Umweltnaturwissenschaften, Albert-Ludwigs-Universität Freiburg, 79104 Freiburg, Germany*
[4]*European Synchrotron Radiation Facility (ESRF), 38043 Grenoble, France*
(Received 11 August 2016; revised manuscript received 12 October 2017; published 20 November 2017)

Correlated x-ray diffraction imaging and light microscopy provide a conclusive picture of three-dimensional dislocation arrangements on the micrometer scale. The characterization includes bulk crystallographic properties like Burgers vectors and determines links to structural features at the surface. Based on this approach, we study here the thermally induced slip-band formation at prior mechanical damage in Si wafers. Mobilization and multiplication of preexisting dislocations are identified as dominating mechanisms, and undisturbed long-range emission from regenerative sources is discovered.

DOI: 10.1103/PhysRevLett.119.215504

Because of growth technologies perfected over many decades, monocrystalline semiconductor wafers are today the most important substrates for microelectronic device fabrication. During thermal processing, any microscopic flaw at the surface may trigger drastic defect generation, and it remains difficult to avoid the plastic deformations caused by the nucleation and expansion of dislocations [1]. These can rapidly evolve into so-called slip bands [2,3], extending considerably into initially dislocation-free substrate areas and entailing large-scale warpage [4] and atomic steps at the surface [5]. With miniaturization reaching the 10 nm technology, such disturbances become increasingly problematic. The depth of focus during deep ultraviolet lithographic patterning and the tolerances for structuring critical elements, e.g., 1 nm for finFET transistors [6], will soon prohibit any degradation of substrate flatness. Also, for the envisaged transition to larger diameter wafers (e.g., from 300 to 450 mm for Si), the control of thermal slip is one important key [7]. Thus, the understanding of its origin and predicting its evolution with suitable theoretical models is of both scientific interest and industrial concern.

In this context, we here propose an approach for correlated three-dimensional (3D) imaging which enables the comprehensive characterization of complex dislocation networks in monocrystals, including the 3D arrangements, the Burgers vectors (BVs), and the interaction among defects and with the surface, altogether providing a precise link between bulk and surface properties. Three imaging methods are combined: x-ray diffraction laminography (XDL) [8], x-ray white-beam topography (XWBT) [9], and (circularly polarized) visible light differential interference contrast (CDIC) microscopy [10]. Complementary to transmission electron microscopy with nanometer resolution [11–13], but restricted to sample thicknesses of a few micrometers or less, we aim for nondestructive 3D access to millimeter-sized crystal volumes with a resolution of a few micrometers, in particular, also compatible with large lateral extensions like, e.g., typical for wafers.

After an overview of the general methodological principles, we will report on an application of the method to the study of slip-band formation in mechanically damaged Si wafers, induced by an exposition to thermal stresses as typical, e.g., for CMOS processing. The observations will be related to the resolved shear stresses (RSS) predicted by models for indentation and annealing, enabling conclusions on the involved mechanisms.

XDL combines x-ray projection topography with principles of laminographic 3D imaging. Similar to tomographic approaches [14], the spatial arrangement of crystal defects is reconstructed from sets of two-dimensional (2D) projection images formed by diffraction contrast (preferably so-called weak-beam contrast [15]) at different view angles. However, the applicability of XDL is extended from rather cylindrical (typical for tomography) to flat samples with considerable lateral extension (as known from conventional laminography [16]). While there is no sensitivity to microscopic properties below the micrometer scale (dissociation into partials, kinks [17], glide or shuffle type [18], etc.), all features of dislocation networks on the "mesoscopic" length scale between a few micrometers and several millimeters are accessible. Individual dislocations are resolved for densities up to 10^7 cm^{-2} even within complex arrangements, where the interpretation of conventional 2D projection topographs is hindered or completely precluded by superposition. The basic concept of XDL is independent of the crystal material. Crystal planes approximately parallel or perpendicular to the surface are not compulsory but allow an improved 3D reconstruction quality, because inconsistencies due to absorption can be compensated [8].

The plastic deformation associated with a dislocation is described by its BV $\mathbf{b}$ [19]. To determine the orientation $\hat{\mathbf{b}} = \mathbf{b}/|\mathbf{b}|$, conventional x-ray diffraction imaging like XWBT exploits the so-called extinction rule [15,20], according to which a reduced topographic contrast of a dislocation within a monocrystal is observed for a reflection from crystallographic hkl planes with diffraction vector $\mathbf{h}_{hkl}$ if $\mathbf{b} \cdot \mathbf{h}_{hkl} = 0$. Thus, $\hat{\mathbf{b}}$ of a selected dislocation follows from the identification of a substantial extinction in at least two reflections $\mathbf{h}_{h_1k_1l_1} \nparallel \mathbf{h}_{h_2k_2l_2}$, leading to $\hat{\mathbf{b}} \propto (\mathbf{h}_{h_1k_1l_1} \times \mathbf{h}_{h_2k_2l_2})$. However, such an evaluation requires the reliable identification of dislocations in topographs for different hkl planes, which for more complex dislocation arrangements is impeded by the increasing superposition in the 2D projections, the high similarity of the individual line objects under consideration, and their very diverse appearance for different view angles. The correlative analysis proposed here overcomes these drawbacks by exploiting the information about the spatial dislocation arrangement from an XDL measurement: The individual 3D paths are extracted from the reconstruction volume, and then a suitable (purely geometrical) forward simulation predicts the location and appearance of the potentially formed contrast in the 2D XWBT images. By direct comparison, e.g., by browsing the digitized XWBT data with virtual overlays of the simulation, now a reliable assessment of the experimental contrast strength is possible. More details about this enhanced BV determination are provided in Supplemental Material [21].

Inherently, a moving dislocation end point creates a well-defined step of $\Delta H = |\mathbf{b} \cdot \mathbf{n}|$ (usually on the order of a few angstroms) along its path at a flat crystal surface (e.g., a polished wafer or a crystal facet) with normal $\mathbf{n}$ [17], the end point of the step marking its final position. CDIC microscopy (in the reflection mode) is known to be well suited for the visualization of such height variations [5]. Based on Ref. [22], we estimate the observable contrast relative to the illumination I_0 to $\Delta I/I_0 \approx 4\pi C \Delta H/\lambda$, with visible light wavelength $\lambda \gg \Delta H$ and an instrumental factor $-1 \leq C \leq 1$. For an ideally adjusted setup ($C = \pm 1$) and typical dislocations in Si (as discussed later), a contrast of about 0.2% is expected, clearly detectable by modern digital camera systems. By comparing the positions of the step line end points in CDIC surface maps with the end points of the 3D dislocation paths extracted from XDL reconstruction, a correlation of the two data sets is possible. Linking in this way the individual dislocations to their surface traces provides a localization at the surface with a few hundred nanometer precision (the resolution of optical microscopy), allows conclusions on the evolutionary history, and relates the internal crystalline defects with any structural features at the surface detectable by CDIC. A more detailed description of the data processing is given in Supplemental Material [21].

Demonstrating the potential of the proposed correlative method, in the following we present its application to the onset of thermal slip in Si wafers. The sample emulates typical damage during industrial processing: A representative, 20×20 mm^2 large piece of a (001)-oriented and 775 μm thick double polished wafer has been nanoindented (Berkovich tip, 400 mN peak force) [23]. Then, rapid thermal annealing up to about 1270 K was performed in a mirror heater during real-time observation by *in situ* XWBT [24], allowing a controlled interruption of the process at a suitably early state of the thermally induced slip-band formation; see Fig. 1(a). For more details about the sample, see Supplemental Material [21], which provides also all relevant experimental parameters.

As illustrated in Fig. 1(c), the characterized dislocation network comprises about 60 interweaved dislocations, surrounding the initial mechanical surface damage. Compared to previous 3D imaging of similar structures [44], the 3D dislocation paths could be determined with about one order of magnitude higher spatial resolution (about 3 μm). Nearly all (98%) of the BV orientations could be identified, and about 95% of the bulk dislocations were successfully linked to their associated surface steps.

The 3D dislocation arrangement determined confirms the current geometrical model of thermal slip in (001)-oriented Si [2,5]: The paths of almost all dislocations lie on the {111} glide planes with straight segments in the

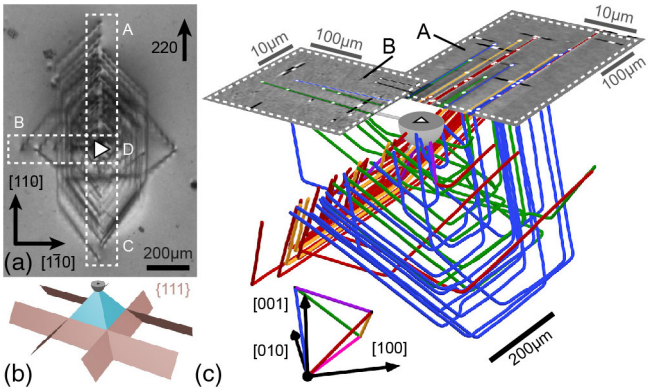

FIG. 1. (a) XWBT image (220 reflection on film) of the sample region investigated. After annealing, the point of indentation (white triangle) is surrounded by a dislocation network. For later reference, the surface regions *A*–*D* are defined [see (c), Fig. 3(a), and Fig. 4(a)]. (b) Illustration of the four {111} slip bands (red, bottom part indicated) containing the 3D paths of all dislocations. The bands mutually intersect nearby the indentation damage and thus leave a pyramidal region directly below dislocation-free (blue). A gray hemisphere depicts the strong deformation surrounding the indentation damage. (c) A 3D rendering based on the combined information from XDL and XWBT, for regions *A* and *B* also indicating the relation to the CDIC surface maps in Fig. 3(a) (see Supplemental Movie [21]). Tubes with a radius of 3 μm (estimated spatial resolution) represent the 3D dislocation paths, and a color code indicates the associated BV orientations determined.

$\langle 110 \rangle$ directions. Additionally, our results reveal that they predominantly form hexagonally shaped half-loops with two end points at the surface. Clearly, these half-loops are exclusively located within four 5–15 μm thick $\{111\}$ slip bands, leaving a pyramidal dislocation-free crystal region below the original damage [Fig. 1(b)]. Surprisingly, the number of dislocations in "opposing" slip bands differs, and the end point positions inside such pairs of bands appear not to be correlated [illustrated by the white dots in Fig. 2(a)]. This clearly indicates the nucleation of independent half-loops, in contradiction to previously proposed models, which suggest a pairwise half-loop emergence on mutually inclined $\{111\}$ glide planes [2].

The color code in Fig. 2(a) illustrates the BV distribution determined. Only $\langle 110 \rangle$ orientations are found, where $|\mathbf{b}| = a\sqrt{2}$ (with lattice constant a) is suggested by crystallographic considerations [19]. Since dissociation into partials takes place below the accessible micrometer scale, here as well as in the later discussions the observable "effective" BVs (corresponding to the linearly superposed elastic deformation) are considered. Several aspects of the distribution can be explained by means of finite element

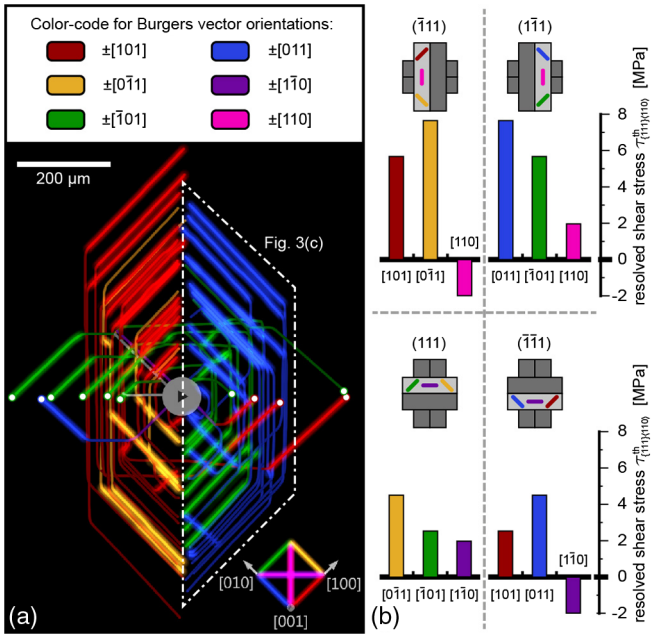

FIG. 2. (a) Top view [compare Fig. 1(a)] on the BV distribution determined, with all screw segments highlighted. Only $\langle 110 \rangle$ orientations are found. White dots mark the surface end points of the dislocations within the (111) and $(\bar{1}\,\bar{1}\,1)$ slip bands, illustrating their uncorrelated appearance. (b) The thermally induced RSS $\tau^{th}_{\{111\}\langle 110\rangle}$ on the 12 $\{111\}\langle 110\rangle$ glide systems (planes and BV orientations indicated in the four schemes), according to FE calculations. Stress values between -2 and 8 MPa are obtained. The systems with the lowest stresses $|\tau^{th}_{\{111\}\langle 110\rangle}|$ fit the suppressed activation for $\mathbf{b} \propto [1\bar{1}0]$ (purple) and $\mathbf{b} \propto [110]$ (pink) observed in (a).

(FE) calculations of the thermal RSS on the 12 $\{111\}\langle 110\rangle$ glide systems, $\tau^{th}_{\{111\}\langle 110\rangle}$, the result shown in Fig. 2(b) (more details in Supplemental Material [21]). In particular, the rare appearance of $\mathbf{b} \propto [1\bar{1}0]$ (purple) and $\mathbf{b} \propto [110]$ (pink) correlates with the low RSS predicted for the corresponding systems. Also, the larger number of defects inside the $(\bar{1}11)$ and $(1\bar{1}1)$ bands fits the expected higher nucleation rate due to stronger driving forces [the top row compared to the bottom row in Fig. 2(b)]. The same argument explains the larger half-loop expansion in the $\pm[110]$ direction [vertical in Fig. 2(a)] compared to $\pm[1\bar{1}0]$ (horizontal). In contrast, our calculations yield the same RSS, e.g., for $(\bar{1}11)[0\bar{1}1]$ and $(1\bar{1}1)[011]$, while the activation observed for these systems differs significantly. Here our assumption of a time-invariant 2D temperature field instead of the experimentally not accessible, but in general time-dependent and 3D distribution turns out to be inadequate for a more realistic modeling (details in Supplemental Material [21]). In the future, precisely determined BV distributions like the one presented may provide valuable data for the further development and verification of more sophisticated calculations, e.g., considering the dynamics of complex physical wafer-heater system as a whole [25].

For all dislocations, the calculated $\mathrm{sgn}(\tau^{th}_{\{111\}\langle 110\rangle})$ in Fig. 2(b) allows concluding on the directionality of the associated microscopic deformation (the signs $\pm\mathbf{b}$), with independent cross-checking enabled by the CDIC contrast of the corresponding surface steps. This reveals that without exception the network collectively shifts the dislocation-free pyramid [blue in Fig. 1(b)] towards the rear side of the wafer. It is essential for the plastic behavior during further heating that all dislocations jointly elevate there a square area (the base of the pyramid) opposite to the original damage [see Fig. 3(d)]. FE simulations with different Gaussian temperature profiles suggest that above the brittle-ductile transition [45,46] this is the general behavior of (001)-oriented Si wafers with surface damage close to the local temperature maxima.

The absence of $\pm[\bar{1}10]$ and $\pm[110]$ BV orientations (parallel to the surface) ensures the previous trajectories of all dislocation end points being reflected by surface step lines. As illustrated in Fig. 3(a) for the $(\bar{1}11)$ and $(1\bar{1}1)$ slip bands, which cross regions A and C, this allows the location of the corresponding active glide planes being investigated with the resolution of CDIC microscopy (about 200 nm). Clusters are revealed, in particular, two main subbands with $(\bar{1}11)[101]$ and $(1\bar{1}1)[011]$ glide systems, respectively [see also Fig. 4(a)]. Furthermore, in some cases common atomic glide planes are suggested for groups of half-loops, like for α, β, and γ highlighted in Fig. 3(c). For these, the identical BV, the high similarity, and the concentric arrangement indicate the activity of a regenerative Frank-Read-type source [47]. Such an undisturbed long-range emission of

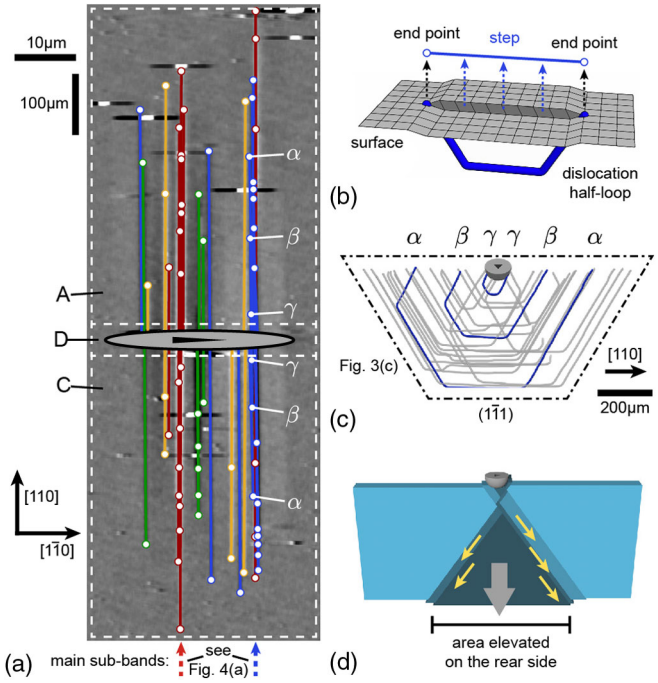

FIG. 3. (a) Surface map of the regions A, C, and D [compare Fig. 1(a)], showing the location of all steps detected in the CDIC data and their relation to the individual dislocations inside the $(\bar{1}11)$ and $(1\bar{1}1)$ slip bands in the bulk below. The visualization is $10\times$ compressed along $\pm[110]$. As illustrated in (b), all steps are represented by lines colored according to the BV of the associated dislocations, the end point positions of which are marked by white dots. (c) Isolated view on the $(1\bar{1}1)$ slip band [see Fig. 2(a)] with the half-loops α, β, and γ highlighted. Identical BV, similarity, concentricity, and end point positions compatible with a common glide plane [indicated in (a)] suggest their emission from a regenerative dislocation source. (d) Macroscopic plastic deformation of the wafer (scheme). The dislocation-free pyramid is moved to the rear side, finally elevating there an undisturbed square area.

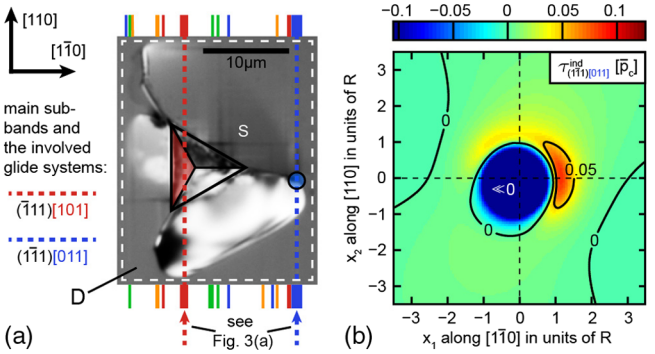

FIG. 4. (a) CDIC micrograph of the indentation damage in region D [see Figs. 1(a) and 3(a)], including the positions of all active glide planes within the $(\bar{1}11)$ and $(1\bar{1}1)$ slip bands. Two main subbands intersect the left facet of the triangular imprint (red) and a crack tip (blue) at the edge of a breakout. At S, many short surface steps are visible. (b) RSS $\tau^{ind}_{(1\bar{1}1)[011]}$ during indentation, calculated using the Hertz contact stress model (contact radius $R = 1$), normalized to the mean contact pressure $\bar{p}_c$, and in a depth of $(R/3)$ below the surface.

dislocations from a single source inside such complex networks is surprising and has not been reported before. Its occurrence may in the future become of considerable industrial relevance, since the pileup of the associated atomic steps quickly leads to local height differences on the order of nanometers, compromising the manufacture and functioning of microelectronic devices with a similar structure size even in wafer areas far from the original damage.

Figure 4(a) shows that all thermally activated glide planes intersect the surface close to the initial damage. For the subband active on $(1\bar{1}1)[011]$ and close to the surface, Fig. 4(b) illustrates the RSS distribution during indentation, $\tau^{ind}_{(1\bar{1}1)[011]}$, calculated by means of the Hertz contact stress model [26]. The highest RSS with $\mathrm{sgn}(\tau^{ind}_{(1\bar{1}1)[011]}) = \mathrm{sgn}(\tau^{th}_{(1\bar{1}1)[011]}) = +1$ [see Fig. 2(b)] appears to the right of the contact area. Thus, here the highest initial nucleation rate is expected for dislocations with a BV orientation and sign likely to be subsequently thermally driven into the wafer bulk, fitting the subband position observed in Fig. 4(a) (dashed blue line). It can also be shown that $\tau^{ind}_{(1\bar{1}1)[011]}(x_1, x_2) = \tau^{ind}_{(1\bar{1}1)[011]}(-x_1, x_2)$, which explains why the other main subband intersects the surface on the opposite side of the indentation center (dashed red line). In contrast, $\tau^{ind} \ll 0$ below the contact area appears to have no observable effect on the thermally driven slip-band formation. This is explained by all relevant $\tau^{th}_{\{111\}\langle 110\rangle} > 0$, which leads to the immediate annihilation of the corresponding dislocations at the surface close to the damage, resulting in the short high surface steps visible as dark contrast around S in Fig. 4(a).

For thermally induced slip-band formation in mechanically damaged Si, our observations do not exclude contributions from homogeneous nucleation of new dislocations (e.g., at stress concentrators). But due to the clear correlation of (i) the preferred positions of slip-band emergence and (ii) the locations with $\mathrm{sgn}(\tau^{th}) = \mathrm{sgn}(\tau^{ind})$ for the corresponding glide systems, the activation of preexisting dislocations (induced during the prior damaging) appears to be the dominating mechanism, including their multiplication by regenerative sources.

In summary, we showed that correlative 3D imaging combining XDL, XWBT, and CDIC data provides comprehensive insight into complex dislocation networks in monocrystalline materials. The 3D paths of dislocations and the associated BV distribution can be precisely determined and correlated with features at the surface, providing a hitherto inaccessible, comprehensive snapshot of plastic deformation processes. For selected regions of large samples like wafers, a 3D spatial resolution of a few micrometers is achieved (about 200 nm at the surface). The

approach is nondestructive and thus suited for future *in situ* studies, e.g., of fundamental activation parameters. Here we relate our observations of thermally driven slip-band formation in damaged Si wafers to theoretical predictions of the driving forces and identify mobilization and multiplication of preexisting dislocations as the dominating mechanisms. The observed long-range emission of dislocations from regenerative sources represents a potential problem for future microelectronic device fabrication.

We thank all members of the SIDAM project consortium, in particular, J. Garagorri, M. R. Elizalde, J. Wittge, D. Allen, P. McNally, B. K. Tanner, and T. Jauß. Also, the various contributions of J. Moosmann, A. Cecilia, V. Weinhardt, and S. Doyle are gratefully acknowledged. The work was supported by the allocation of beam time MI-1079 at the ESRF and partially funded by EU-FP7 Project No. 216382 "SIDAM" and by the German Bundesministerium für Bildung, Forschung und Technologie Grant No. 05K14VFA "STROBOS-CODE."

*daniel.haenschke@kit.edu

[1] A. Fischer, G. Kissinger, G. Ritter, V. Akhmetov, and M. Kittler, Mater. Sci. Eng. B **159–160**, 103 (2009).
[2] J. Wittge, A. N. Danilewsky, D. Allen, P. McNally, Z. Li, T. Baumbach, E. Gorostegui-Colinas, J. Garagorri, M. R. Elizalde, D. Jacques, M. C. Fossati, D. K. Bowen, and B. K. Tanner, J. Appl. Crystallogr. **43**, 1036 (2010).
[3] B. K. Tanner, J. Wittge, D. Allen, M. C. Fossati, A. N. Danilewsky, P. McNally, J. Garagorri, M. R. Elizalde, and D. Jacques, J. Appl. Crystallogr. **44**, 489 (2011).
[4] J. M. Yi, Y. S. Chu, T. S. Argunova, J. Z. Domagala, and J. H. Je, J. Synchrotron Radiat. **15**, 96 (2008).
[5] A. N. Danilewsky, J. Wittge, A. Cröll, D. Allen, P. McNally, P. Vagovič, T. d. S. Rolo, Z. Li, T. Baumbach, E. Gorostegui-Colinas, J. Garagorri, M. R. Elizalde, M. C. Fossati, D. K. Bowen, and B. K. Tanner, J. Cryst. Growth **318**, 1157 (2011).
[6] K. Schuegraf, M. Abraham, A. Brand, M. Naik, and R. Thakur, IEEE J. Electron Device Soc. **1**, 66 (2013).
[7] B. Tanner, J. Wittge, P. Vagovič, T. Baumbach, D. Allen, P. McNally, R. Bytheway, D. Jacques, M. Fossati, D. Bowen, J. Garagorri, M. Elizalde, and A. Danilewsky, Powder Diffr. **28**, 95 (2013).
[8] D. Hänschke, L. Helfen, V. Altapova, A. Danilewsky, and T. Baumbach, Appl. Phys. Lett. **101**, 244103 (2012).
[9] T. Tuomi, K. Naukkarinen, and P. Rabe, Phys. Status Solidi A **25**, 93 (1974).
[10] R. Danz and P. Gretscher, Thin Solid Films **462–463**, 257 (2004).
[11] J. C. H. Spence, H. R. Kolar, G. Hembree, C. J. Humphreys, J. Barnard, R. Datta, C. Koch, F. M. Ross, and J. F. Justo, Philos. Mag. **86**, 4781 (2006).
[12] J. S. Barnard, J. Sharp, J. R. Tong, and P. A. Midgley, Science **313**, 319 (2006).
[13] C.-C. Chen, C. Zhu, E. R. White, C.-Y. Chiu, M. C. Scott, B. C. Regan, L. D. Marks, Y. Huang, and J. Miao, Nature (London) **496**, 74 (2013).
[14] W. Ludwig, P. Cloetens, J. Härtwig, J. Baruchel, B. Hamelin, and P. Bastie, J. Appl. Crystallogr. **34**, 602 (2001).
[15] A. Authier, *Dynamical Theory of X-Ray Diffraction* (Oxford University, New York, 2004).
[16] L. Helfen, T. Baumbach, P. Mikulík, D. Kiel, P. Pernot, P. Cloetens, and J. Baruchel, Appl. Phys. Lett. **86**, 071915 (2005).
[17] D. Hull and D. J. Bacon, *Introduction to Dislocations* (Butterworth-Heinemann, Amsterdam, 2011).
[18] M. S. Duesbery and B. Joos, Philos. Mag. Lett. **74**, 253 (1996).
[19] J. P. Hirth and J. Lothe, *Theory of Dislocations* (McGraw-Hill, New York, 1968).
[20] D. K. Bowen and B. K. Tanner, *High Resolution X-Ray Diffractometry and Topography* (Taylor & Francis, London, 1998).
[21] See Supplemental Material at http://link.aps.org/supplemental/10.1103/PhysRevLett.119.215504 for more detailed information about the methodology and the application case presented, which includes Refs. [2,3,5, 8–10,15,17,19,20,22–43].
[22] J. S. Hartman, R. L. Gordon, and D. L. Lessor, Appl. Opt. **19**, 2998 (1980).
[23] J. Garagorri, E. Gorostegui-Colinas, M. R. Elizalde, D. Allen, and P. McNally, An. Mec. Fract. **27**, 559 (2010).
[24] A. N. Danilewsky, J. Wittge, A. Hess, A. Cröll, D. Allen, P. McNally, T. D. Rolo, P. Vagovič, T. Baumbach, J. Garagorri, M. Elizalde, and B. K. Tanner, Phys. Status Solidi A **208**, 2499 (2011).
[25] J. Garagorri, M. R. Elizalde, M. C. Fossati, D. Jacques, and B. K. Tanner, J. Appl. Phys. **111**, 094901 (2012).
[26] C. Atkinson, J. M. Martinez-Esnaola, and M. R. Elizalde, Mater. Sci. Technol. **28**, 1079 (2012).
[27] H. Saka and G. Nagaya, Philos. Mag. Lett. **72**, 251 (1995).
[28] D. Allen, J. Wittge, A. Zlotos, E. Gorostegui-Colinas, J. Garagorri, P. J. McNally, A. N. Danilewsky, and M. R. Elizalde, Nucl. Instrum. Methods Phys. Res., Sect. B **268**, 383 (2010).
[29] T. Jauß, A. Danilewsky, J. Wittge, A. Cröll, J. Garagorri, R. M. Elizalde, D. Allen, and P. McNally, Cryst. Res. Technol. **47**, 253 (2012).
[30] A. Danilewsky, J. Wittge, A. Hess, A. Cröll, D. Allen, P. McNally, P. Vagovič, A. Cecilia, Z. Li, T. Baumbach, E. Gorostegui-Colinas, and M. R. Elizalde, Nucl. Instrum. Methods Phys. Res., Sect. B **268**, 399 (2010).
[31] A. N. Danilewsky, J. Wittge, A. Rack, T. Weitkamp, R. Simon, T. Baumbach, and P. McNally, J. Mater. Sci. **19**, 269 (2008).
[32] A. N. Danilewsky, A. Rack, J. Wittge, T. Weitkamp, R. Simon, H. Riesemeier, and T. Baumbach, Nucl. Instrum. Methods Phys. Res., Sect. B **266**, 2035 (2008).
[33] A. Rack, T. Weitkamp, S. B. Trabelsi, P. Modregger, A. Cecilia, T. dos Santos Rolo, T. Rack, D. Haas, R. Simon, R. Heldele, M. Schulz, B. Mayzel, A. Danilewsky, T. Waterstradt, W. Diete, H. Riesemeier, B. Müller, and T. Baumbach, Nucl. Instrum. Methods Phys. Res., Sect. B **267**, 1978 (2009).

[34] T. Weitkamp, P. Tafforeau, E. Boller, P. Cloetens, J.-P. Valade, P. Bernard, F. Peyrin, W. Ludwig, L. Helfen, and J. Baruchel, AIP Conf. Proc. **1221**, 33 (2010).
[35] L. Helfen, A. Myagotin, P. Mikulík, P. Pernot, A. Voropaev, M. Elyyan, M. Di Michiel, J. Baruchel, and T. Baumbach, Rev. Sci. Instrum. **82**, 063702 (2011).
[36] A. Myagotin, A. Voropaev, L. Helfen, D. Hänschke, and T. Baumbach, IEEE Trans. Image Process. **22**, 5348 (2013).
[37] M. H. Longair, D. A. Baker, and J. D. Armstrong, Bioinformatics **27**, 2453 (2011).
[38] J. Schindelin, I. Arganda-Carreras, E. Frise, V. Kaynig, M. Longair, T. Pietzsch, S. Preibisch, C. Rueden, S. Saalfeld, B. Schmid, J.-Y. Tinevez, D. J. White, V. Hartenstein, K. Eliceiri, P. Tomancak, and A. Cardona, Nat. Methods **9**, 676 (2012).
[39] X. R. Huang, J. Appl. Crystallogr. **43**, 926 (2010).
[40] D. L. Lessor, J. S. Hartman, and R. L. Gordon, J. Opt. Soc. Am. **69**, 357 (1979).
[41] J. Laugier and B. Bochu, OrientExpress software package, 2001.
[42] J. J. Hall, Phys. Rev. **161**, 756 (1967).
[43] K. L. Johnson, *Contact Mechanics* (Cambridge University Press, Cambridge, England, 2003).
[44] D. Allen, J. Wittge, J. Stopford, A. Danilewsky, and P. McNally, J. Appl. Crystallogr. **44**, 526 (2011).
[45] C. S. John, Philos. Mag. **32**, 1193 (1975).
[46] P. B. Hirsch and S. G. Roberts, Philos. Mag. A **64**, 55 (1991).
[47] F. C. Frank and W. T. Read, Phys. Rev. **79**, 722 (1950).